



Effect of energy density on the interface evolution of stainless steel 316L deposited upon INC 625 via directed energy deposition

D. R. Feenstra^{1,2,*} , A. Molotnikov³ , and N. Birbilis⁴ 

¹Department of Materials Science and Engineering, Monash University, Room 109, Level 1, 22 Alliance Lane (Building 69), Clayton, VIC 3800, Australia

²Woodside Innovation Centre, Monash University, Clayton, VIC 3800, Australia

³RMIT Centre for Additive Manufacturing, School of Engineering, Royal Melbourne Institute of Technology, Melbourne, VIC 3053, Australia

⁴College of Engineering & Computer Science, The Australian National University, 108 North Road, Canberra, ACT 2601, Australia

Received: 27 February 2020

Accepted: 2 June 2020

Published online:

9 June 2020

© Springer Science+Business Media, LLC, part of Springer Nature 2020

ABSTRACT

Directed energy deposition (DED) is an additive manufacturing technique that permits the manufacturing of complex multi-material components. In the present study, DED was used for the fabrication of Inconel 625 and stainless steel 316L couples. The effect of input energy density on the evolution of the dissimilar metal interface and its mechanical properties was explored by varying the laser power for each build. Columns that transitioned directly from Inconel 625 to stainless steel 316L were deposited onto mild steel substrates. The columns were cross-sectioned and characterised by coupling physical characterisation with microhardness. Scanning electron microscopy and compositional mapping were used to correlate the relationship between energy density and the produced functional gradient. It was seen that high energy deposition resulted in a measurable, remelted layer solute (RLS) fraction that comprised each deposited layer, creating a stepwise-graded interface. The RLS fraction was consistent across each layer of the interface and was influenced by the energy density of the build. Changes in the RLS affected the length of the graded interface but did not have a significant influence the mechanical properties. The yield strength and ultimate tensile strength of the through-interface compared well with the traditional wrought stainless steel 316L but suffered in ductility. Mix-mode fracture tended to occur in the near stainless steel composition regions.

Address correspondence to E-mail: darren.feenstra@monash.edu

Introduction

Additive manufacturing (AM) has emerged as an advanced manufacturing method for fabrication of complex engineering designs. Amongst the various AM techniques, directed energy deposition (DED) offers unique capabilities of manufacturing large and complex multi-material components. The concept of fabrication of multi-material parts is not entirely new, but the joining of dissimilar metals remains challenging. The effect of the processing condition on the formation of the interfaces and their mechanical properties is not well understood, while dissimilar metal welding using shielded metal arc welding and gas tungsten arc welding [1–4] has been the subject of many studies using these methods which have inherent limitations, such as the requirement of particular filler materials, and also subject to inducing large heat affected zones (HAZs) during fabrication [1–4]. Alternatively, non-fusion welding techniques such as explosion bonding or friction-stir welding nominally offer mechanically bonded interfaces which may have variations in strength compared to the base materials [3, 5].

Conversely, DED presents high potential for dissimilar metal bonding, due to the ability to tailor the processing parameters and make use of the localised deposition of the material and powder laser interaction [6]. Modern DED systems can incorporate multiple feed hoppers that can be utilised to manipulate the input composition and offering the ability to produce graded structures and in situ alloying. Several studies have explored this concept to fabricate functionally graded materials (FGMs) by DED using following materials couples: pure Ti- to Ti-based alloys [7–9], Ti alloys to Fe-based alloys [10, 11], steel to stainless steel [12] and stainless steel- to Ni-based alloys [13].

Liu et al. [7] demonstrated the use of in situ powder mixing to fabricate TiC/Ti FGMs: it was shown that gradual transitions could produce crack-free composites, while direct transitions to Ti-95vol%TiC composite resulted in vertical cracks, and long transverse cracks in a Ti-80vol%TiC composite direct transition. Cracking was attributed to high levels of thermal stress and interfacial mismatch stresses that formed during the process. Mahamood et al. [8] showed how DED could be used to optimise FGM fabrication, by optimising the parameters for each deposited layer in the transition. Li et al. [11]

attempted to join Ti6Al4V and SS316 via DED but experienced severe cleavage fracture due to strong intermetallic formation. Li et al. [10, 11] designed a new transition based on the principal alloying elements transitioning as follows: Ti6Al4V → V → Cr → Fe → SS316, effectively mitigating the intermetallic defect formation.

Farren et al. [12] investigated the feasibility of joining carbon steel to stainless steel via DED. It was seen that a smooth transition could be produced with four distinct microstructure regions in the joint: austenite, dual-phase austenite/martensite, ferrite/bainite and tempered martensite. Solidification cracks were prone to form in the austenitic region that could be mitigated by adjusting the composition range to ensure solidification of primary ferrite and secondary austenite to minimise the occurrence of hot cracking. Shah et al. [13] used parametric design to test continuously graded SS316L and Inconel 718 thin walls via DED. The laser power and powder mass flow rates were tested to understand their impact on the produced microstructure and mechanical properties. It was seen that the tensile strength of the transition was inversely proportional to the laser power and increased with powder mass flow rate, most likely due to changes in cooling rates. Carroll et al. [14] graded from SS304L to Inconel 625 over 24 layers via DED. The approach resulted in a smooth transition without sharp compositional changes or microstructural boundaries. Cracks were observed in the 80% SS304L region. Using thermodynamic calculations, they were able to determine that this region corresponded with conditions for stable monocarbide nucleation. EDS mapping-revealed cracked areas were rich in Mo and Nb, suggesting that Monocarbide (Mo, Nb) was the main culprit for solidification cracking. Chen et al. [15] did an in-depth analysis of the microstructure development of an SS316L and Inconel 625 FGM fabricated by DED. They were able to achieve excellent mechanical properties (yield strength and UTS of 822.77 and 1029.9 MPa, respectively) by grading the transition in 10% increments. It was seen that the primary alloying elements, Fe and Ni, were able to homogeneously diffuse for each layer. With increasing Inconel 625 content, the primary dendrites increased in thickness and secondary arm spacing. When the composition exceeded 80% Inconel 625, secondary phases formed along the dendritic boundary. Failure in the joint was attributed to micropore rupture.

In this study, the joining of Inconel 625 (INC625) and stainless steel 316L (SS316L) via melt pool mixing is explored. Inconel and stainless steel have the potential for good bonding as they are both primarily single phase, face-centred cubic (FCC) structures that share many of their principal alloying elements (Ni, Fe, Cr) that have mutual solid solubility. There have been many attempts to join Inconel and stainless steel together, primarily through the use of different fusion welding techniques in which many challenges quickly become apparent: firstly, during welding, Inconel alloys become prone to forming detrimental α -chromium precipitates in the fusion zone (FZ) and HAZ, inducing hot cracking [16, 17]. Secondly, microfissuring or microcracking, in the HAZ, can form due to large heat inputs, leading to poor mechanical properties in the weld [18]. Additionally, Nb-rich phases can precipitate during welding that can induce embrittlement and result in a reduction in ductility, fracture toughness and fatigue [17, 19].

Several traditional fusion welding approaches require the use of filler materials [17, 20–23]. The selection of suitable filler material is based on finding a filler with a thermal expansion coefficient between the two substrate materials and one which can create a strong metallurgical bonding with both materials. Furthermore, the filler needs to have high solubility. To date, there is no clear front runner filler material as each selection suffers from particular deficiencies. Often the use of simpler alloys than one of the substrate materials is preferred to limit the effect of excessive precipitation of the alloying elements.

In this work, the use of melt pool mixing in the DED process is explored for the creation of functionally graded materials. The melt pool can be manipulated in size by changing the energy density which depends on the processing parameters such as laser power, scan speed and beam size. The interplay between these parameters is assessed by considering the dilution rate. In welding, the dilution rate is defined as the fraction of the weight of the remelted substrate vs the whole weight of the weld [3, 4]. A similar concept is adopted for DED where the dilution rate is used to describe the fraction of the previous layer that is remelted and combined with the deposited layer. In DED systems, the dilution ratio is affected by the ratio between the energy density and the material deposition rate. A DED process with a high energy density and a low deposition rate results in a deep penetrating melt pool. In general welding, it

is desirable to avoid high dilution rates as they can result in adverse effects such as hard spots, embrittlement and cracks [3]. Here, it will be demonstrated that high dilution rates may be a beneficial approach to produce functional gradient materials with tunable compositional changes.

Materials and methods

Two materials, namely Inconel 625 (INC 625) and stainless steel 316L, were used in this study.

The metal powders were supplied by TLS Technik with a spherical shape with an average size of 70 μm within a range between 50 and 100 μm . The compositions of both powders are reported in Table 1.

Columns with the dimensions of $15 \times 15 \times 20 \text{ mm}^3$ were fabricated on a mild steel substrate using a Trumpf TruLaser cell 7040 DED system. The printing parameters are summarised in Table 2.

In each build, the base of the column was built from INC 625 to a height of 10 mm and then transitioned immediately to 10 mm of stainless steel 316L. All printing was conducted within a controlled atmosphere by pumping helium to purge the oxygen levels below 20 ppm. Columns were printed using a constant set of printing parameters only varying the laser power between 1200 and 2000 W.

Characterisation

The samples were cross-sectioned down the middle of each column, parallel to build direction via wire cutting. The samples were ground to a 4000 grit surface finish and then polished to 1 μm surface finish using diamond paste. A Duramin A300 hardness tester was used with a 200-g load and 10 s dwell time to measure the Vickers hardness across the welds. Measurements were taken every 0.5 mm parallel to the build direction, along the left, centre and right thirds of the column. The sampling length was condensed across the weld zone to 0.25 mm, with an 0.25 mm alternating stagger in the X direction, to achieve better resolution. The profiles across the welds were plotted and the average Vickers hardness was calculated from the bulk regimes of each material.

The opposite cross sections, likewise, were ground to a 4000 grit surface finish and then polished to a 1 μm surface finish using diamond pastes and then

Table 1 Powder compositions supplied by TLS Technik

Element (wt%)	Fe	Cr	Ni	Mo	Mn	Si	C	Nb
Inconel 625	0.33	21.5	Bal	9.1	0.42	0.45	0.001	3.62
SS 316L	Bal	16.6	11.5	2.2	0.9	0.6	0.02	-

Table 2 Printing parameters used in test matrix

Parameter	Condition
Laser Power (W)	1200,1400,1600,1800,2000
Laser focus/diameter	2 mm
Laser scan/traverse speed	800 mm/min
Build Height	0.44 mm
Hatch spacing	2 mm (50%)
Powder supply rate	3 rpm (~ 10 g/min)

finished with colloidal silica suspension (OPS). These cross sections were examined using a JEOL 7001F FEG scanning electron microscope (SEM) with an accelerating voltage of 30 keV and a working distance of 10 mm. All imaging was done using the backscatter detector to attain a composition image. Elemental mapping was collected using standard energy-dispersive X-ray spectroscopy (EDS) techniques. Ten elemental line scans were collected via EDS across the weld zones to attain average compositional profiles of the interface for each sample.

To test the mechanical properties of each interface, $20 \times 60 \times 60 \text{ mm}^3$ test blocks were printed using the same conditions as the test columns. The test blocks were sectioned into 60-mm sub-size tensile bars via wire cutting. The samples were tested using an Instron Model 4505/5500R tensile frame with a 10 kN load cell and 0.02 strain rate. A minimum of seven tensile bars were tested for each condition, and their results were reported as stress–strain curves. Additionally, the average yield strength and ductility results were collected for each build condition.

Results

Hardness profiles

Hardness profiles revealed that there were consistent levels of hardness in the bulk regimes as shown in the representative hardness profiles in Fig. 1a. In each

sample, the hardness decreased rapidly at the interface as it transitioned from the Inconel to the stainless steel side. The profiles were staggered to show that the transition zone lengthened with the increase in laser power. These hardness profiles were then used to establish the relationship between bulk hardness and laser power as shown in Fig. 2b. It can be seen that the average microhardness of the bulk INC 625 was $260 \pm 13 \text{ HV}$, while the bulk SS 316L was $157 \pm 5 \text{ HV}$. It was seen that with increasing laser power, the bulk hardness of INC 625 dropped from $272 \pm 14 \text{ HV}$ at 1200 W to $233 \pm 11 \text{ HV}$ at 2000 W. The bulk hardness of SS 316L decreased similarly from $172 \pm 9 \text{ HV}$ at 1200 W to $144 \pm 8 \text{ HV}$ at 2000 W. This decrease in hardness is unsurprising as increased laser power would result in larger melt pool dimensions, prolonged solidification times and therefore larger grain sizes. Increased laser power also resulted in greater shape deformation at the top of the columns.

Microstructural characterisation

Each interface was assessed by SEM, revealing a functionally graded interface. Backscatter electron (BSE) imaging in Fig. 2 of a cross-sectioned sample produced at 1200 W reveals characteristic features found in each interface. In each build, it was seen that the produced microstructure was very dense and minimal porosity was found, even at high magnification. The interface was marked by high contrast between the Inconel and stainless steel sides, especially across the first dissimilar layer. As labelled Fig. 2a, the individual melt pools can be clearly seen via BSE imaging. This allows for direct quantification of the effect of the printing parameters on the resulting weld size, layer thickness and bead overlap. Typical layer designation is numbered from the first dissimilar layer to the bulk area as shown in Fig. 2b. The layers can be differentiated by the melt pool boundaries.

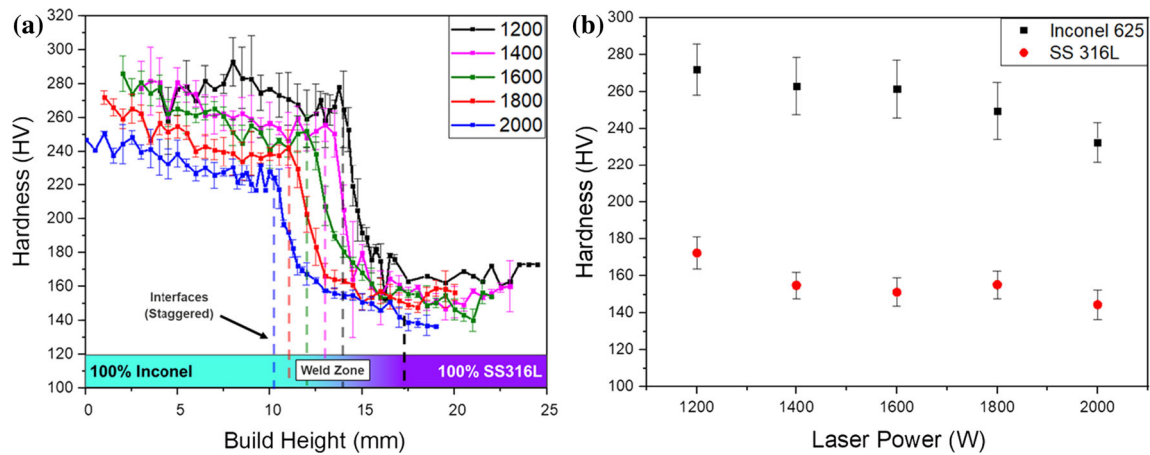


Figure 1 Effect of laser power on hardness of Inconel 625 and Stainless Steel 316L bonded via DED: **a** Staggered average microhardness line profiles across weld interface for each laser

power (W), with the interface regimes designated by dashed vertical lines, **b** Bulk microhardness trends for each material vs laser power.

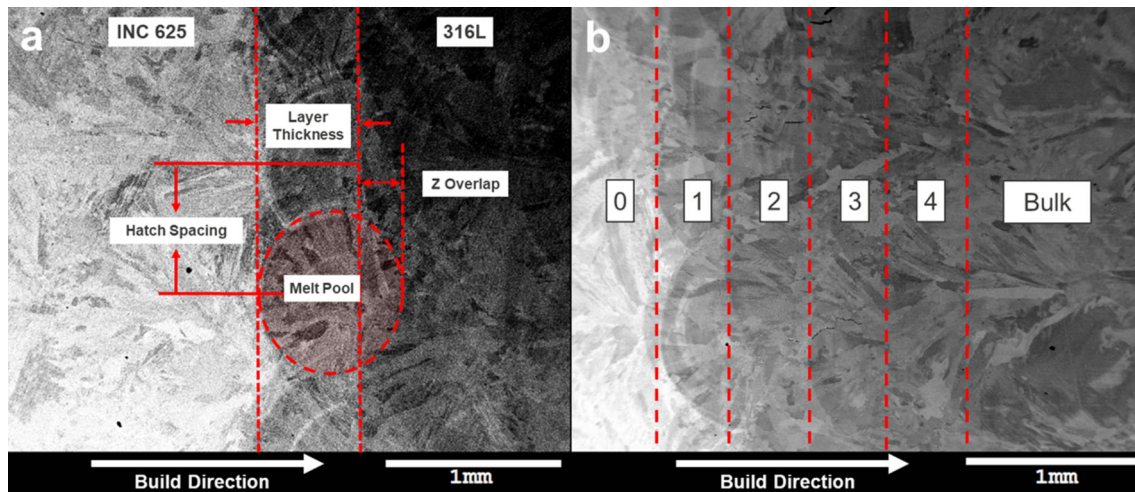


Figure 2 Inconel 625 and stainless steel interface fabricated via DED, BSE imaging of interface produced with 1200 W: **a** Key interface characteristics, **b** Layer designation.

Compositional distribution across dissimilar metal interface

Energy-dispersive X-ray spectroscopy mapping revealed the elemental distribution across each weld with minimal elemental diffusion across the melt pool boundaries, see Fig. 3. The melt pools were marked by distinct rings of Ni-rich regions around the bottom edges of the Fe-rich melt pools, which can be understood by mass transport of remelted Inconel that deposited around the edges of the molten SS 316L pool. This is similar to the wicking effect seen in welding which was reported when stainless steel 316L was deposited onto Inconel 690 [24]. It is worth noting that this wicking effect was not seen in the

reverse build (both reported and studied). Although the origins of wicking have not been thoroughly characterised to date, the effect can be rationalised by noting the difference in melting temperatures between stainless steel 316L (1375–1440 °C) and Inconel (1290–1350 °C) [25] resulting in partial melting and capillary action along the melt pool boundary. Each layer is partially ablated as deposition of the subsequent layer induces remelting and mixing. Due to the use of a bidirectional scan pattern, one would expect to see an alternating grain morphology in the build direction. However, it was observed that the perpendicular scanning direction layer (vertical to the page) was fully consumed by the primary scanning direction (through the page). The dominant

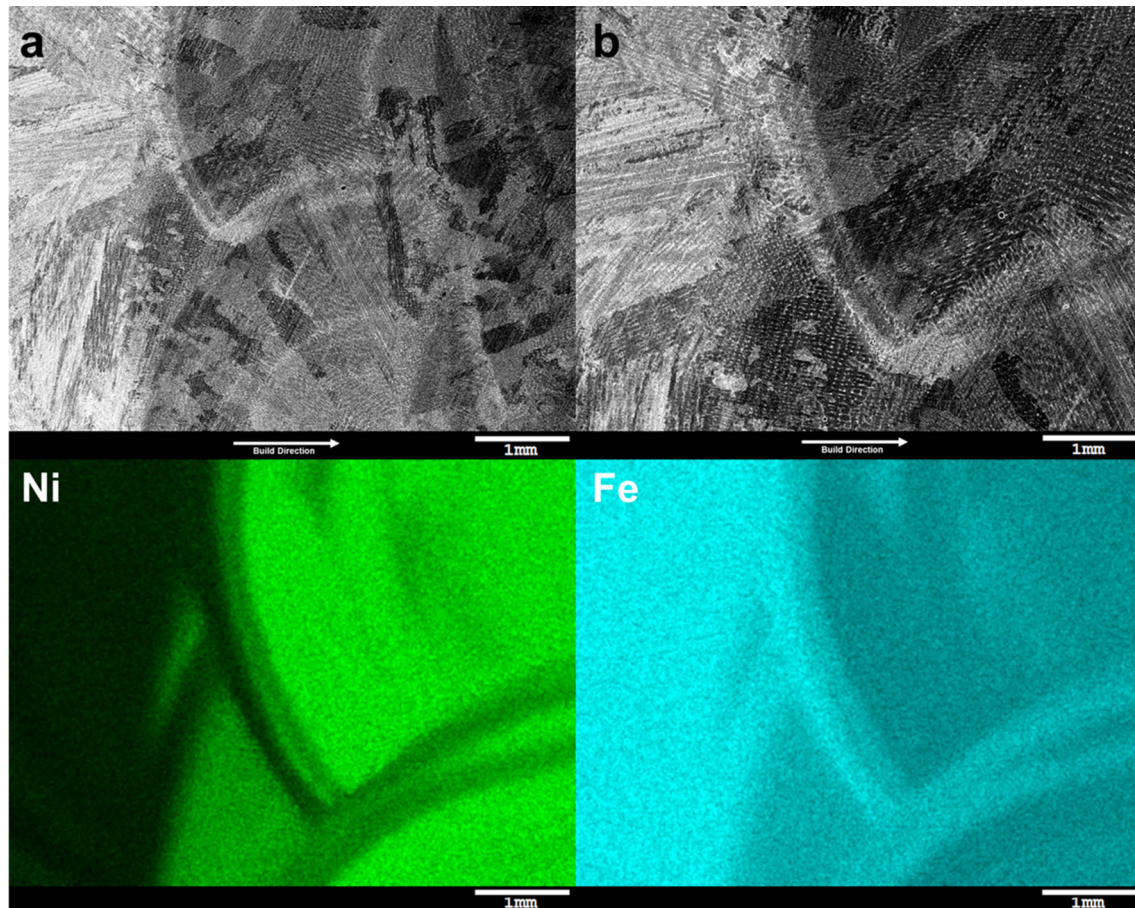


Figure 3 Compositional mapping of Fe and Ni across the initial dissimilar melt interface of 3D-printed stainless steel 316L onto Inconel 625 at 1400 W showing the wicking effect along the edges of the melt pools.

scanning direction seen depends on the section plane taken, suggesting that a grain memory texturing effect dominates epitaxial growth locally in a two-layer (~ 0.9 mm) area.

Compositional maps were collected across the interface of each sample for the laser power range. Each map revealed distinct layers that gradually transitioned from the bulk to bulk as demonstrated in Fig. 4a. The first layer is representative of the bulk Inconel 625 with every subsequent layer being a layer in the transition zone. Typical EDS line profiles across the interface printed at 2000 W are shown in Fig. 4b, indicating that each layer (~ 0.9 mm) had a characteristic elemental composition forming a stepwise functional gradient. Abnormalities in each local layer were the result of the measured wicking. In subsequent layers, the wicking effect becomes less pronounced in its frequency and composition difference to the measured local bulk.

Mechanical behaviour

Tensile testing was conducted across the interface to test the mechanical response of the bond. Typical stress–strain curves for each laser power are shown in Fig. 5a: each condition measured responded similarly to a typical single material test, with a linear yield regime. After plastic deformation commenced, each condition experienced strain hardening up to the UTS and quick subsequent failure. Tensile testing revealed that the interface had an average yield strength of 398 ± 33 MPa and UTS levels of 564 ± 31 MPa (Fig. 5b) across the laser powers used. These properties are higher than those typically found in wrought 316L [25]. Ductility at maximum load had high levels of variance and averaged 10–15% which was much lower than that typical of wrought 316L [25]. For each laser power tested, there was limited variance in yield stress and UTS, but higher levels of variance of the strain measured at

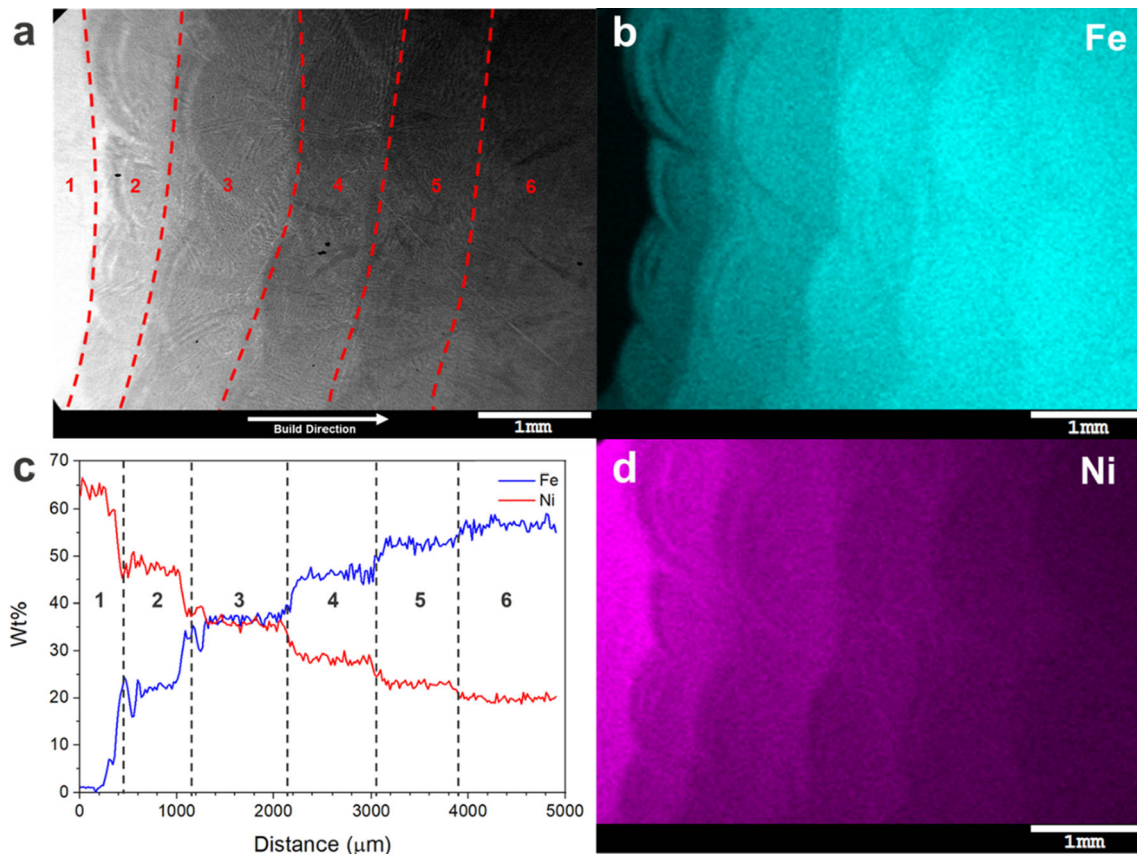


Figure 4 Compositional mapping and line profiles revealing a distinct functional gradient formed with 2000 W laser deposition: **a** Interface imaging with layer designation, with the layer 1 and 2

boundary representing the interface between the bulk Inconel 625 and the weld zone, **b** Fe distribution, **c** Typical compositional line profile and **d** Ni Distribution.

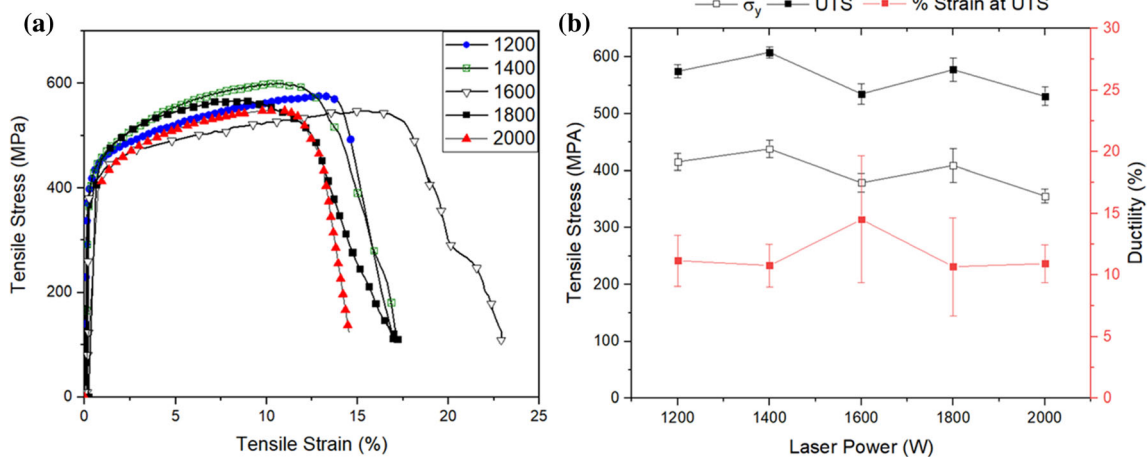


Figure 5 Results of mechanical testing across interface: **a** Representative tensile curves for each laser power (W), **b** Influence of laser power on the mechanical properties across the interface.

fracture. There was a slight, nonlinear, negative trend between increased laser power and yield strength and UTS. The yield and UTS measured for the 1400 W condition were the highest, but the lowest for

the 2000 W condition. There was no meaningful trend between laser power and ductility. Each tensile specimen showed preferential deformation and uneven necking, favouring the stainless steel side of

the interface: the stainless steel side formed strain striations from the necking region to the end of the gauge, while the Inconel side underwent less necking. Fracture typically occurred at the interface on the stainless steel side in the layers that contained bulk compositions comparable to stainless steel 316L.

Discussion

Effect of energy input on interface evolution

For each condition, the average interface/gradient length was measured by measuring the distance between the bulk composition of the Inconel 625 and the bulk composition of the stainless steel 316L. These measurements were taken from both the Fe and Ni concentration, the two primary exchange elements at the interface. The average interface length was measured and plotted against laser power as shown in Fig. 6.

The dilution of the Inconel composition layer to layer is affected by the fraction of the previous layer that is remelted and mixed with pure stainless 316L in the melt pool during deposition. This fraction was calculated by taking the marginal change in Ni and Fe concentration and calculating a mass balance between the composition of the previous layer and the material being deposited (C_D). The calculation of the remelted layer solute fraction (RLS) is reduced to the following:

$$RLS = \frac{C_i - C_D}{C_{i-1} - C_D} \quad (1)$$

It was seen that there was a decaying positive correlation between the increase in laser power and increase in interface length: as the laser power increased above 1600 W, its influence on the measured interface length diminished. At lower power levels, increasing laser power can result in higher build rates [26] due to the energy input in well below the required energy threshold to melt the amount of powder supplied to the laser. At higher power ranges, when the supplied energy input exceeds the threshold requirement, the build height will not increase, while the melt pool will continue to grow in length, width [26–28] and depth [17]. More importantly, it has been reported that the dilution fraction exponentially grows with the increase in laser power [28]. This results in an increased amount of remelting of the previous layer later resulting in an increase in the RLS fraction leading to a more gradual transition between the bulk compositions at the interface. As expected, the RLS fraction had a positive correlation with laser power but dropped off after 1800 W possibly due to laser attenuation.

Effect of microstructure on mechanical response

As mentioned previously, increasing laser power results in an increase of the length of the interface. However, it was noted that these changes to the length of the interface had no substantial effect on the mechanical response as shown in Fig. 5b. In general, the average measured yield strength (398 ± 33 MPa) and UTS (564 ± 31 MPa) were superior to pure stainless steel 316L in the wrought (170 and 485 MPa, respectively) [25] and the cast equivalent, SA-351 CF3M, (205 and 482 MPa, respectively) [29] and comparable to other studies of DED-fabricated 316L [30–32]. The mechanical properties achieved were comparable with other attempts to weld Inconel and stainless steel: Devendranath Ramkumar et al. [20] explored the use of different filler materials using continuous current gas tungsten arc welding (CCGTAW) and pulsed current gas tungsten arc welding (PCGTAW) techniques to combine 316L with Inconel 718. Their best results were achieved using CCGTA welding and ERNiCu-7 achieving a yield and tensile strength of 346 and 624 MPa,

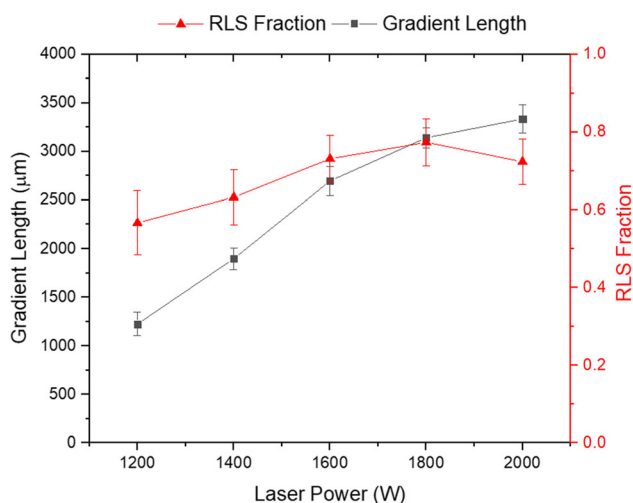


Figure 6 Influence of laser power on the length of the measured gradient zone and on the remelted layer solute fraction.

respectively [20]. Zhang et al. showed recently with the use of premixed powders joined 316L and Inconel 625 with the use of low power DED. They were successfully able to achieve a yield strength of 405.6 MPa and a UTS 605.7 MPa. Similarly, necking and fracture occurred in the stainless regime of the joint [33]. Increasing laser power had little impact on ductility resulting in values between 10 and 15% which were much lower than that found in pure 316L wrought (40%) [25] and cast SA-351 CF3M (30%) [29] and lower than that achieved with DED by Zhang et al. (43%) [33].

Intermetallic formation

Embrittlement in welding stainless and Inconel alloys together is often blamed on brittle intermetallics formed in the interface during welding. With the addition of Fe content in the transition layers, the solubility of Mo and Nb decreased within the γ -austenite matrix [34, 35], increasing the susceptibility of the formation of detrimental phases such as Laves phase (Fe_2Nb) and NbC carbides [36, 37]. Despite the rapid solidification process, the interface was not free of segregation: high-resolution investigation of the microstructures revealed the formation of Nb- and Mo-rich precipitates. BSE imaging of the second layer of the transition at 2000 W in Fig. 7 revealed extensive segregation of the Nb and Mo from the Fe-rich γ -austenite matrix to form cell structures. There was no

distinct distribution of Ni and Cr, suggesting that phases formed were primarily γ'' - Ni_3Nb enriched with Mo.

Site of tensile failure

To correlate the reduction in ductility to the local microstructure, sections normal to the fracture location were taken to observe its relation to the transition. It was found that the location of fracture occurred in the sixth–tenth layer of the transition, well into the bulk regime confirmed by bulk EDS measurements made just below the fracture area shown in Fig. 8. Furthermore, microscopy revealed a low density of γ'' precipitates in the area below the fracture area with no signs of Cr enrichment. The fracture was jagged in nature joggling as much as 1 mm in vertical variance. The location of fracture suggested that embrittlement could not be attributed to intermetallic formation.

Investigation of the fracture surfaces from the tensile specimens taken from across the interface revealed a mixed mode fracture as shown in Fig. 9. The fracture area was divided by macro-scale cleavage cracks varying in size and direction. Between the cracks, large areas with characteristic, ductile non-homogenous dimples were found as shown in Fig. 9b. The dimples varied in size with a few as large as 5 μm , while the majority were smaller than 1 μm in size corresponding with the size of the micro-voids

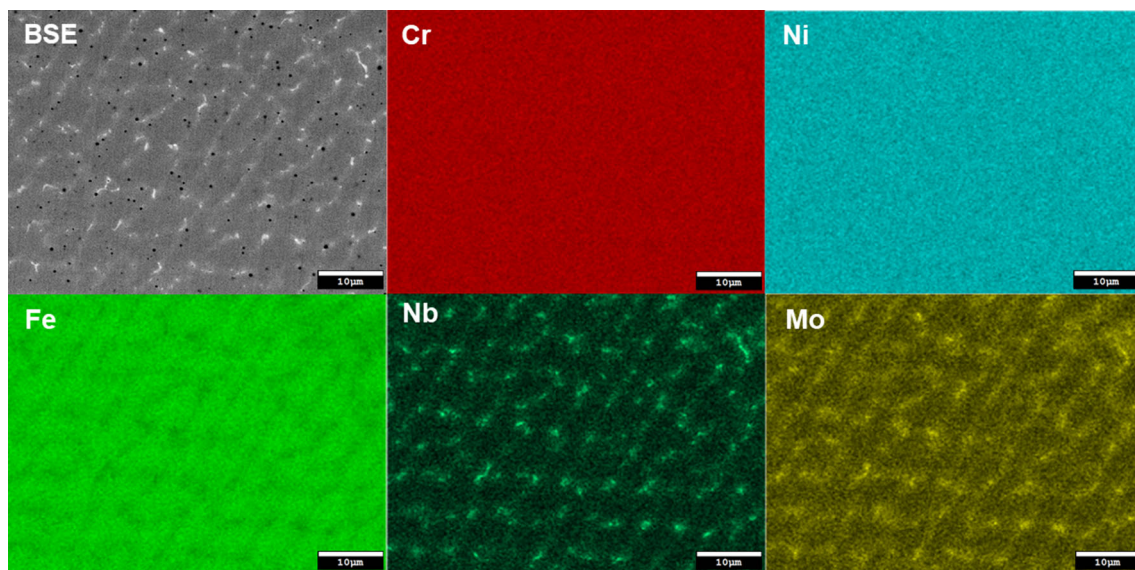


Figure 7 High magnification compositional mapping of layer #2 printed at 2000 W revealing Nb–Mo-rich segregation from Fe-rich solute.

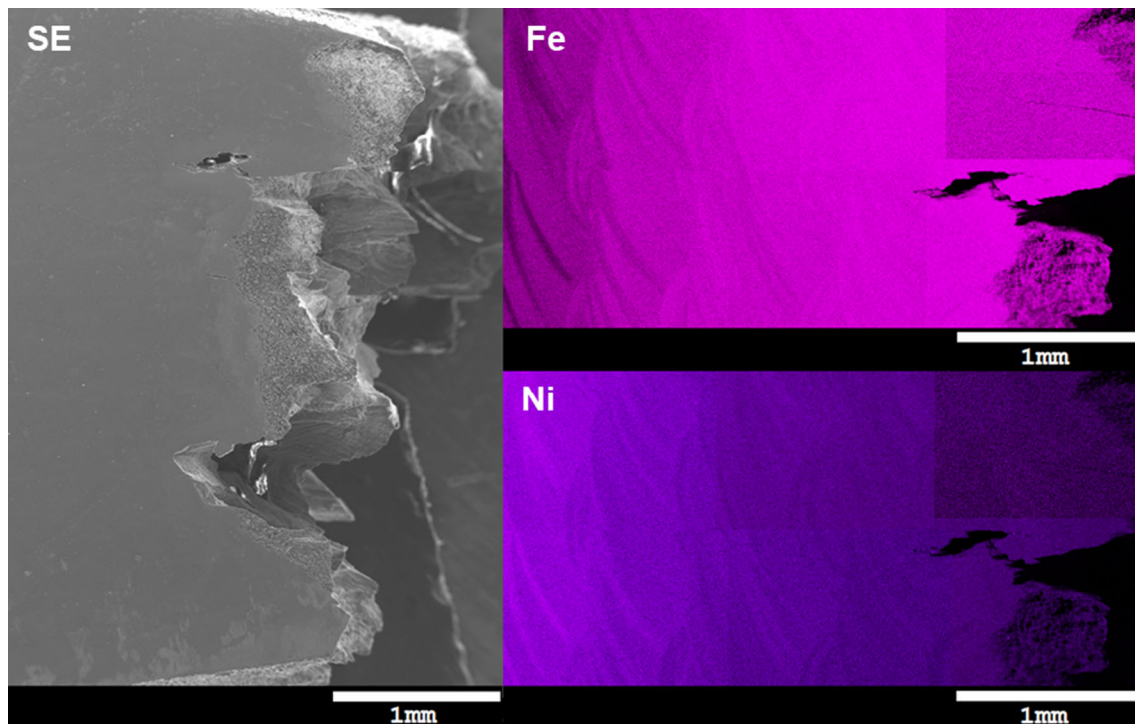


Figure 8 Location of fracture with respect to the interface on a pulled tensile specimen from a printed sample printed at 2000 W. Fracture typically traversed layers 6–10, in areas with bulk compositions near stainless steel 316L.

typical of the DED printing process (Fig. 7). The ductile areas ended at the edges of the cracks marked by a thin boundary of quasi-cleavage surfaces. The fracture surface inside the cracks was transgranular in nature with small nodes. As shown in Fig. 10, the cracks had a groove-like morphology parallel to the crack plane and the build direction.

Grain morphology

Inspection of the grain morphology across the Inconel–stainless steel interface revealed a bi-modal grain size distribution as shown in Fig. 11. Despite elemental segregation showing distinct layers, large columnar grains, millimetres in size, formed across several layers of deposition on an angle to the build direction. Many of the large grains had sharp kinks which turned in direction, suggesting some thermal epitaxy effects on grain growth. Surrounding the large columnar grains were small micron-sized grains. This highly, bi-modal grain structure would have direct effects on the ductility and the mixed fracture mode of the interface. Large columnar growth could be mitigated through manipulation of the scan strategy, the addition of inoculants elements

[38, 39] and increasing layer dwell time [30, 40]. In some of the samples, a few solidification cracks were observed at the end of the transition zone in the near bulk stainless steel zone, which could have also attributed to premature fracture as they would act as stress concentrators, reducing the maximum achievable UTS and strain at fracture.

Conclusions

The study herein explored the use of melt pool mixing to create a functional gradient between Inconel 625 and stainless steel 316L. The main conclusions are summarised below:

Deposited layers consisted of a mixture of the previous (underlying) layer that was remelted and mixed via the melt pool of deposited 316L stainless steel. The fraction of the remelted layer solute (RLS) was as high as ~65%, at higher laser power levels. At the edge of the melt pools, there was evidence of limited diffusion (mass transport) in the form of wicking, indicating that the extent of melt pool mixing is highly related to the temperature of the melt pool and the location of its isotherms.

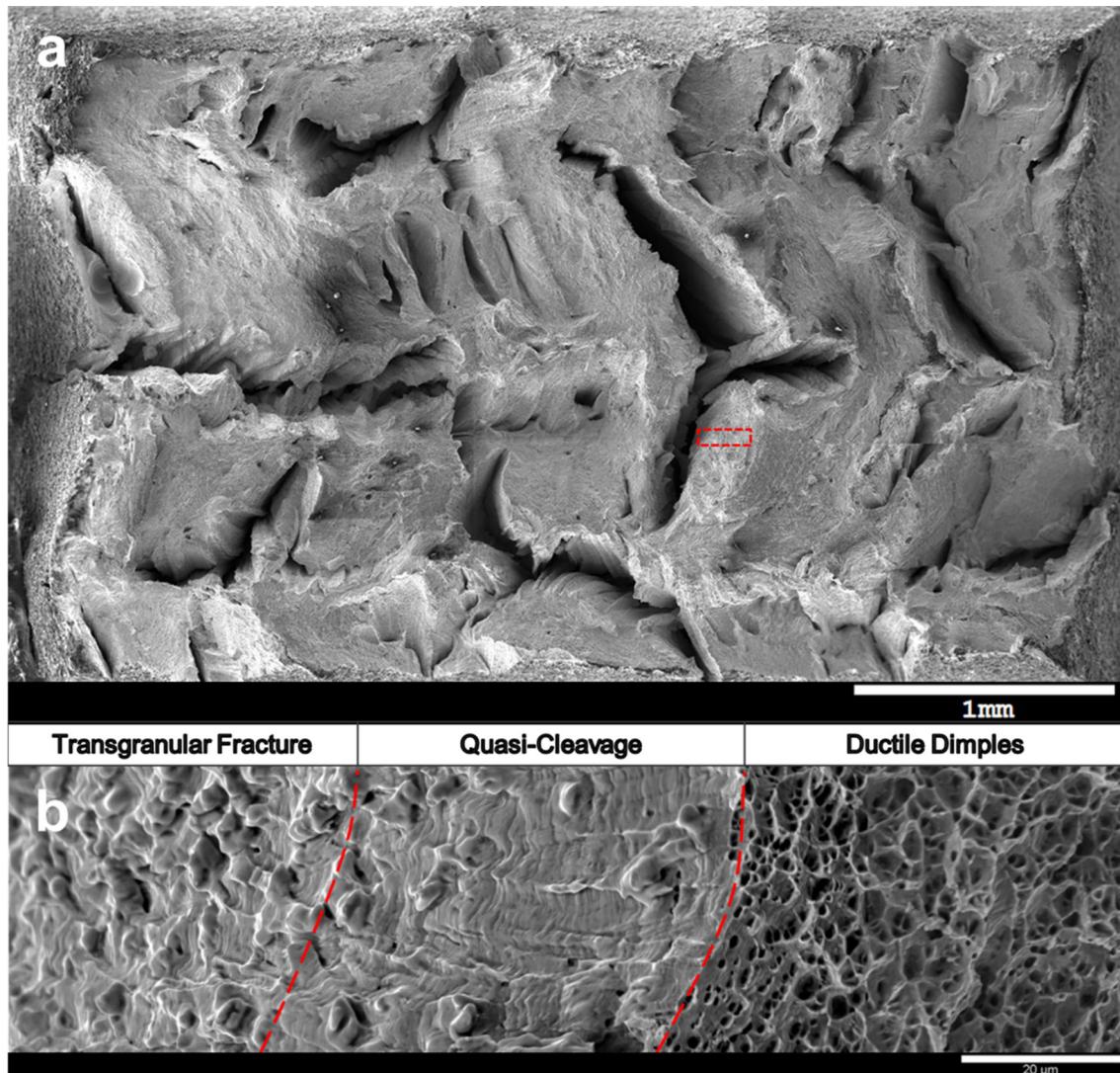


Figure 9 a Fracture surface of pulled tensile specimen taken through the Inconel–stainless interface of a sample printed with 2000 W. b High magnification imaging of fracture across the boundary between ductile regions and brittle macro-scaled cracks.

Melt pool mixing resulted in the formation of compositionally graded interfaces, in which each deposited layer possessed a local composition, creating a stepwise compositional gradient. Variances in the composition profiles were attributed to wicking.

The remelted layer solute fraction could be calculated from the intermediate changes in composition between layers. The remelted layer solute fraction was consistent across the interface and could be manipulated by changing laser power.

Increasing the laser power in the DED process from 1200 to 2000 W resulted in the widening of the compositional gradient up to 3.5 mm. The combination of increased layer height and RLS fraction

resulted in gradual, wider compositional gradients, but had no major effect on the mechanical properties.

The through-thickness mechanical properties of the interface were higher than recorded values for wrought stainless steel 316L in terms of yield strength and UTS. However, the interface suffered from embrittlement with significantly lower ductility than that typical of wrought stainless 316L.

The formation of γ'' -Ni₃Nb precipitates enriched with Mo was found in the compositional transition zone, with the highest γ'' density in regions where the fraction between stainless steel and Inconel was approximately 50–50. With increasing Fe content, the extent of segregation of Nb and Mo increased; however, ductility loss was not correlated with γ''

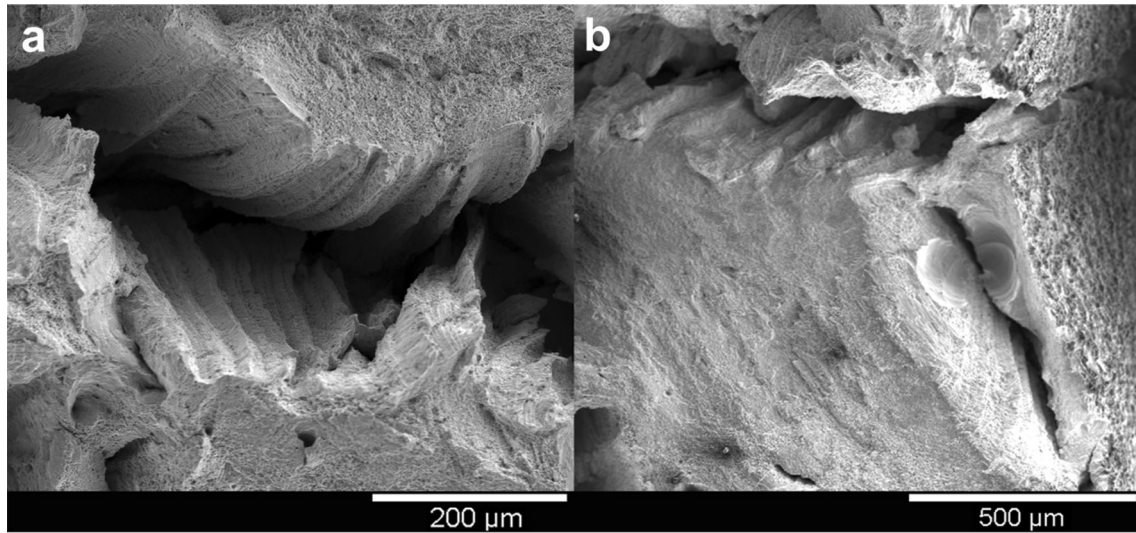
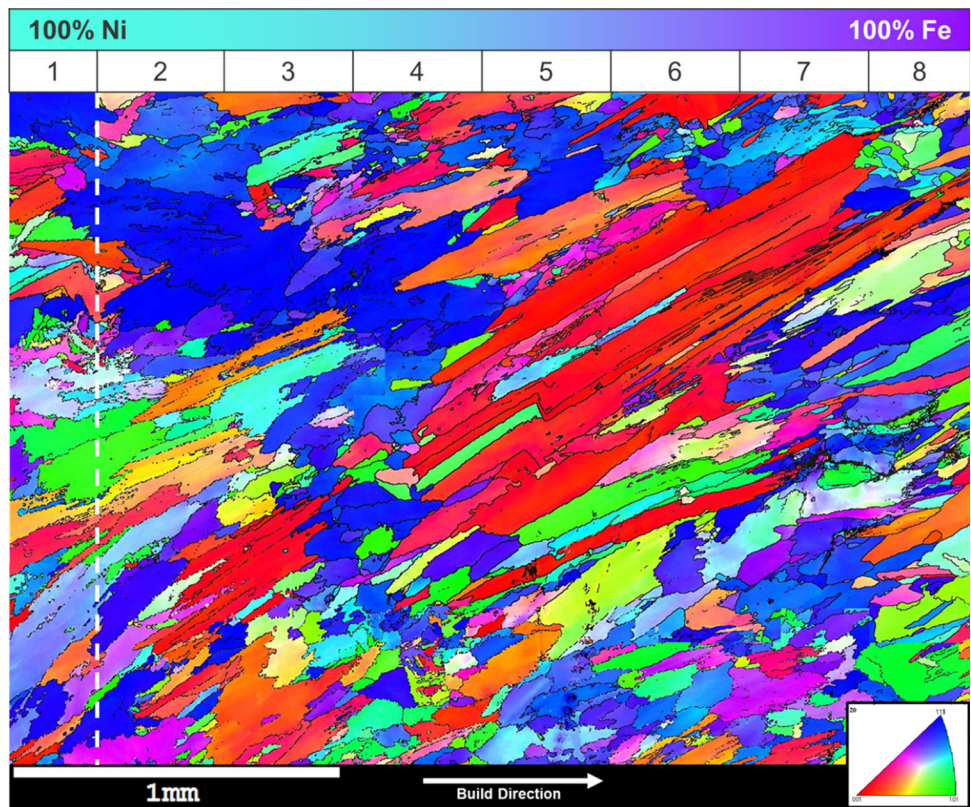


Figure 10 Characteristic features in fracture surface: **a** Groove-like morphology of the macro-scaled cracks, **b** Ruptured void aiding in crack formation.

Figure 11 Grain morphology montage taken across Inconel–stainless steel interface for a sample printed with a laser power of 2000 W showing the bi-modal grain size distribution.



precipitation as fracture sites were located in near the bulk stainless side of the interface where the precipitation density was lowest.

The tensile fracture mode as determined following tensile testing was so-called ‘mixed’, with large areas of homogenous ductile dimpling divided by macro-

scale cracks revealing transgranular fracture surfaces. The areas between the ductile dimpling and transgranular fracture were marked with a thin boundary of quasi-cleavage. Cracks were jagged with some evidence of void rupture, possibly due to pre-existing solidification cracks.

The grain morphology of the interface was bi-modal in nature with large columnar grains on the order of millimetres in size that crossed several deposition layers despite the change in composition and time-distinct melting, and solidification. Columnar grains grew on an angle to build direction and had several sharp jogs indicating epitaxial influences. Surrounding the columnar grains were smaller micron-sized, equiaxed grains. This bi-modal grain structure is attributed to the mixed mode fracture and responsible for the reduction in ductility.

Acknowledgements

We gratefully acknowledge the support of the Monash Centre for Electron Microscopy (MCEM), the Monash Centre for Additive Manufacturing (MCAM) and Woodside Energy.

Author contributions

DF was involved in conceptualisation, methodology, formal analysis, investigation writing—original draft preparation, writing—review & editing. AM was involved in conceptualisation, review & editing and supervision. NB was involved in conceptualisation, methodology, writing—review & editing, supervision, project administration and funding acquisition.

Compliance with ethical standards

Conflict of interest The authors declare that they have no known competing financial interests or personal relationships that could have appeared to influence the work reported in this paper.

References

- [1] Lundin CD (1982) Dissimilar metal welds-transition joints literature review, Weld Res Suppl. https://files.aws.org/wj/supplement/WJ_1982_02_s58.pdf.
- [2] Sun Z, Ion JC (1995) Laser welding of dissimilar metal combinations. *J Mater Sci* 30:4205–4214. <https://doi.org/10.1007/BF00361499>
- [3] Messler RW (1999) Principles of welding, Wiley. New York. <https://doi.org/10.1002/9783527617487>
- [4] Ramakrishnan P (1972) Welding metallurgy, Wiley. New York. <https://doi.org/10.22486/iwj.v4i3.150243>
- [5] Cai W, Daehn G, Vivek A, Li J, Khan H, Mishra RS, Komarasamy M (2019) A state-of-the-art review on solid-state metal joining. *J. Manuf. Sci. Eng. Trans. ASME*. <https://doi.org/10.1115/1.4041182>
- [6] Shamsaei N, Yadollahi A, Bian L, Thompson SM (2015) An overview of direct laser deposition for additive manufacturing; Part II: mechanical behavior, process parameter optimization and control. *Addit Manuf* 8:12–35. <https://doi.org/10.1016/j.addma.2015.07.002>
- [7] Liu W, DuPont JN (2003) Fabrication of functionally graded TiC/Ti composites by laser engineered net shaping. *Scr Mater* 48:1337–1342. [https://doi.org/10.1016/S1359-6462\(03\)00020-4](https://doi.org/10.1016/S1359-6462(03)00020-4)
- [8] Mahamood RM, Akinlabi ET (2015) Laser metal deposition of functionally graded Ti6Al4V/TiC. *Mater Des* 84:402–410. <https://doi.org/10.1016/j.matdes.2015.06.135>
- [9] Wang F, Mei J, Wu X (2006) Microstructure study of direct laser fabricated Ti alloys using powder and wire. *Appl Surf Sci* 253:1424–1430. <https://doi.org/10.1016/j.apsusc.2006.02.028>
- [10] Li W, Liou F, Newkirk J, Brown Taminger KM, Seufzer WJ (2017) Investigation on Ti6Al4V-V-Cr-Fe-SS316 multi-layers metallic structure fabricated by laser 3D printing. *Sci Rep* 7:1–14. <https://doi.org/10.1038/s41598-017-08580-z>
- [11] Li W, Yan L, Karnati S, Liou F, Newkirk J, Taminger KMB, Seufzer WJ (2017) Ti-Fe intermetallics analysis and control in joining titanium alloy and stainless steel by laser metal deposition. *J Mater Process Technol* 242:39–48. <https://doi.org/10.1016/j.jmatprotec.2016.11.010>
- [12] Farren JD, DuPont JN, Noecker FF (2007) Fabrication of a carbon steel-to-stainless steel transition joint using direct laser deposition—a feasibility study. *Weld J* 86:55–61
- [13] Shah K, ul Haq I, Khan A, Shah SA, Khan M, Pinkerton AJ (2014) Parametric study of development of Inconel-steel functionally graded materials by laser direct metal deposition. *Mater Des* 54:531–538. <https://doi.org/10.1016/j.matdes.2013.08.079>
- [14] Carroll BE, Otis RA, Borgonia JP, Suh JO, Dillon RP, Shapiro AA, Hofmann DC, Liu ZK, Beese AM (2016) Functionally graded material of 304L stainless steel and inconel 625 fabricated by directed energy deposition: characterization and thermodynamic modeling. *Acta Mater* 108:46–54. <https://doi.org/10.1016/j.actamat.2016.02.019>
- [15] Chen B, Su Y, Xie Z, Tan C, Feng J (2020) Development and characterization of 316L/Inconel625 functionally graded material fabricated by laser direct metal deposition. *Opt Laser Technol* 123:105916. <https://doi.org/10.1016/j.optlastec.2019.105916>
- [16] Belloni G, Caironi G, Gariboldi A, Lo Conte A, Bovisa C (2001) Effect of microstructural alteration on the creep

- behaviour and effect of flaws in 50Cr50Ni-nb engineering alloy. In: SMiRT 16, pp 1–8
- [17] Naffakh H, Shamanian M, Ashrafzadeh F (2009) Dissimilar welding of AISI 310 austenitic stainless steel to nickel-based alloy Inconel 657. *J Mater Process Technol* 209:3628–3639. <https://doi.org/10.1016/j.jmatprotec.2008.08.019>
- [18] Agilan M, Krishna SC, Manwatkar SK, Eg V, Sivakumar D, Pant B (2012) Effect of welding processes (GTAW & EBW) and solutionizing temperature on microfissuring tendency in inconel 718 welds. *Mater Sci Forum* 710:603–607. <https://doi.org/10.4028/www.scientific.net/MSF.710.603>
- [19] Caironi G, Gariboldi E, Silva G, Vedani M (1994) Influence of preliminary heat treatments on microstructure, mechanical properties and creep behaviour of a 50Cr-50Ni niobium containing alloy. *Mater Sci Forum* 163–6:181–188. <https://doi.org/10.4028/www.scientific.net/msf.163-165.181>
- [20] Devendranath Ramkumar K, Patel SD, Sri Praveen S, Choudhury DJ, Prabakaran P, Arivazhagan N, Xavier MA (2014) Influence of filler metals and welding techniques on the structure-property relationships of Inconel 718 and AISI 316L dissimilar weldments. *Mater Des* 62:175–188. <https://doi.org/10.1016/j.matdes.2014.05.019>
- [21] Bansal A, Sharma AK, Das S, Kumar P (2016) On microstructure and strength properties of microwave welded Inconel 718/ stainless steel (SS-316L). In: *Proc. Inst. Mech. Eng. Part L J. Mater. Des. Appl.* pp 939–948. <https://doi.org/10.1177/1464420715589206>
- [22] Lin CM (2013) Relationships between microstructures and properties of buffer layer with Inconel 52M clad on AISI 316L stainless steel by GTAW processing. *Surf Coatings Technol* 228:234–241. <https://doi.org/10.1016/j.surfcoat.2013.04.035>
- [23] Ramkumar T, Selvakumar M, Narayanasamy P, Begam AA, Mathavan P, Raj AA (2017) Studies on the structural property, mechanical relationships and corrosion behaviour of Inconel 718 and SS 316L dissimilar joints by TIG welding without using activated flux. *J Manuf Process* 30:290–298. <https://doi.org/10.1016/j.jmapro.2017.09.028>
- [24] Griffith ML, Harwell LD, Romero JT, Schlienger E, Atwood CL, Smugeresky JE (1997) Multi-material processing by LENS™, *Proc. 8th Solid Free. Fabr. Symp.* 387–394
- [25] ASM International (2018) Gray iron In: *Met. Handb. Desk Ed.*, ASM International, Materials Park, OH, pp 309–314. <https://doi.org/10.31399/asm.hb.mhde2.a0003107>
- [26] Zhang K, Liu W, Shang X (2007) Research on the processing experiments of laser metal deposition shaping. *Opt Laser Technol* 39:549–557. <https://doi.org/10.1016/j.optlastec.2005.10.009>
- [27] Ocylok S, Alexeev E, Mann S, Weisheit A, Wissenbach K, Kelbassa I (2014) Correlations of melt pool geometry and process parameters during laser metal deposition by coaxial process monitoring. *Phys Procedia* 56:228–238. <https://doi.org/10.1016/j.phpro.2014.08.167>
- [28] Hofman JT, De Lange DF, Pathiraj B, Meijer J (2011) FEM modeling and experimental verification for dilution control in laser cladding. *J Mater Process Technol* 211:187–196. <https://doi.org/10.1016/j.jmatprotec.2010.09.007>
- [29] ASM International. Handbook Committee, ASM Handbook, Volume 15, 9th Editio, ASM International, 2008. <https://doi.org/10.31399/asm.hb.v15.9781627081870>
- [30] Yadollahi A, Shamsaei N, Thompson SM, Seely DW (2015) Effects of process time interval and heat treatment on the mechanical and microstructural properties of direct laser deposited 316L stainless steel. *Mater Sci Eng A* 644:171–183. <https://doi.org/10.1016/j.msea.2015.07.056>
- [31] Guo P, Zou B, Huang C, Gao H (2017) Study on microstructure, mechanical properties and machinability of efficiently additive manufactured AISI 316L stainless steel by high-power direct laser deposition. *J Mater Process Technol* 240:12–22. <https://doi.org/10.1016/j.jmatprotec.2016.09.005>
- [32] Zheng B, Zhou Y, Smugeresky JE, Schoenung JM, Lavernia EJ (2008) Thermal behavior and microstructure evolution during laser deposition with laser-engineered net shaping: Part II. Experimental investigation and discussion. *Metall Mater Trans A Phys Metall Mater Sci* 39:2237–2245. <https://doi.org/10.1007/s11661-008-9566-6>
- [33] Zhang X, Chen Y, Liou F (2019) Fabrication of SS316L-IN625 functionally graded materials by powder-fed directed energy deposition. *Sci Technol Weld Join* 24:504–516. <https://doi.org/10.1080/13621718.2019.1589086>
- [34] Khayat ZR, Palmer TA (2018) Impact of iron composition on the properties of an additively manufactured solid solution strengthened nickel base alloy. *Pa State Univ.* <https://doi.org/10.1016/j.msea.2018.01.112>
- [35] DuPont JN, Robino CV, Michael JR, Nous MR, Marder AR (1998) Solidification of Nb-bearing superalloys: Part I. Reaction sequences. *Metall Mater Trans A Phys Metall Mater Sci* 29:2785–2796. <https://doi.org/10.1007/s11661-998-0319-3>
- [36] Murr LE, Martinez E, Gaytan SM, Ramirez DA, MacHado BI, Shindo PW, Martinez JL, Medina F, Wooten J, Ciscel D, Ackelid U, Wicker RB (2011) Microstructural architecture, microstructures, and mechanical properties for a nickel-base superalloy fabricated by electron beam melting. *Metall Mater Trans A Phys Metall Mater Sci* 42:3491–3508. <https://doi.org/10.1007/s11661-011-0748-2>
- [37] Cieslak M (1991) The welding and solidification metallurgy of alloy 625. *Weld J* 70:49

- [38] Zhang D, Qiu D, Gibson MA, Zheng Y, Fraser HL, StJohn DH, Easton MA (2019) Additive manufacturing of ultrafine-grained high-strength titanium alloys. *Nature* 576:91–95. <https://doi.org/10.1038/s41586-019-1783-1>
- [39] Collins PC, Brice DA, Samimi P, Ghamarian I, Fraser HL (2016) Microstructural control of additively manufactured metallic materials. *Annu Rev Mater Res* 46:63–91. <https://doi.org/10.1146/annurev-matsci-070115-031816>
- [40] Bontha S, Klingbeil NW, Kobryn PA, Fraser HL (2009) Effects of process variables and size-scale on solidification microstructure in beam-based fabrication of bulky 3D structures. *Mater Sci Eng A* 513–514:311–318. <https://doi.org/10.1016/j.msea.2009.02.019>

Publisher's Note Springer Nature remains neutral with regard to jurisdictional claims in published maps and institutional affiliations.